Ultrasonics Sonochemistry 82 (2022) 105893

Contents lists available at ScienceDirect

Ultrasonics Sonochemistry

journal homepage: www.elsevier.com/locate/ultson

Dependence of wetting on cavitation during the spreading of a filler droplet on the ultrasonically agitated Al substrate

Zhengwei Li, Zhiwu Xu *, Peng He *, Zhongwei Ma, Shu Chen, Jiuchun Yan

State Key Laboratory of Advanced Welding and Joining, Harbin Institute of Technology, Harbin 150001, China

ARTICLE INFO

Keywords:
Wetting
Cavitation
Spreading
Acoustic pressure
Bubble dynamics

ABSTRACT

The cavitation characteristics during the spreading of a pure Sn liquid droplet subjected to ultrasonication were studied for the first time through high-speed photography to reveal the wetting mechanism. Ultrasonic vibration realized the spreading of Sn droplet on the nonwetting pure Al substrate. However, the oxide layer of the substrate at the spreading front is difficult to remove. The high-speed photography result shows that a noncavitation region consistently appears at the spreading front, because the acoustic pressure is below the cavitation threshold of 1.26 MPa. In particular, the width of the noncavitation region gradually increases as the size of the spreading area increases. Such a result accounts for the condition wherein the oxide layer at the spreading front is difficult to remove. Furthermore, the bubble density during spreading gradually decreases due to the decreased acoustic pressure of the thinned liquid. Finally, the bubble dynamics were calculated to verify the wetting mechanism.

1. Introduction

Ultrasonic melt processing has attracted considerable research interest and has extensively been used in various industries [1,2]. One important application of ultrasonic melt processing is ultrasonic-assisted soldering [3]. During this process, a solder droplet spreads on a substrate and wets it within an extremely short time [4]. Wetting is realized by removing the oxide layer on the surface of the substrate [5]. Since its first development, ultrasonic-assisted soldering has been successfully used to join various types of materials, such as Al alloys [6,7], Mg alloys [8], Ti alloys [9], ceramics [10,11], and sapphire. However, the mechanism of oxide layer removal via ultrasonication remains unclear.

Related to the above, the fundamental mechanism underlying this process is acoustic cavitation [12]. During ultrasonic-assisted soldering, the sonotrode generates high-frequency oscillations in the solder; this condition can result in the nucleation, growth, oscillation, collapse of cavitation bubbles, and acoustic streaming [13–15]. The collapse of cavitation bubbles give rise to various unique phenomena, such as local extremely high temperature, high pressure, microjet, and shock wave [16–25]. Such phenomena can rapidly remove the oxide layers on the surface of the substrate [26–28].

Given this background, studying the cavitation characteristics of liquid solder is of great importance [29,30]. However, the main phenomena and mechanisms of acoustic cavitation within liquid metals remain unclear. The direct observation of the cavitation characteristics inside liquid metals is extremely difficult due to the opacity of these metals. In recent years, some researchers have applied synchrotron X-ray imaging to observe the cavitation characteristics in liquid metals [31–38]. Huang et al. [31] observed the cavitation characteristics inside Al-10Cu liquid and reported that the cavitation bubbles are approximately one order of magnitude larger than those found in aqueous solutions due to the high acoustic pressure in the aluminum melt. Xu et al. [32] found that the cavitation bubbles inside Al-10Cu liquid have an average size of approximately 15.3 ± 0.5 μm. Wang et al. [35] studied the bubble variation process inside Bi-8Zn liquid and observed shock waves after bubble collapse. However, synchrotron X-ray imaging technology has several drawbacks. First, it is usually operated at several dozens of frames per second (fps) [31,38]. Low fps rates cannot accurately record the changes in cavitation bubbles within one acoustic period (T) (the ultrasonic frequency is usually higher than 20 kHz), because most cavitation bubbles have lifetimes shorter than 1 T [39]. Thus far, only Mi's group has achieved ultrafast synchrotron X-ray imaging (up to 271,554 fps, such high image acquisition rate is the fastest X-ray imaging beamline in the world [36]) on the dynamics of ultrasonic bubbles and acoustic flow in liquid metals as well as their effects on the solidification microstructures [35,37]. Second, the images acquired by synchrotron X-ray imaging reflect the superimposed images of all cavitation bubbles in the liquid obtained along a specific direction [37].

* Corresponding author.
E-mail addresses: xuzw@hit.edu.cn (Z. Xu), hithepeng@hit.edu.cn (P. He).

https://doi.org/10.1016/j.ultsonch.2021.105893
Received 13 October 2021; Received in revised form 22 December 2021; Accepted 23 December 2021
Available online 24 December 2021

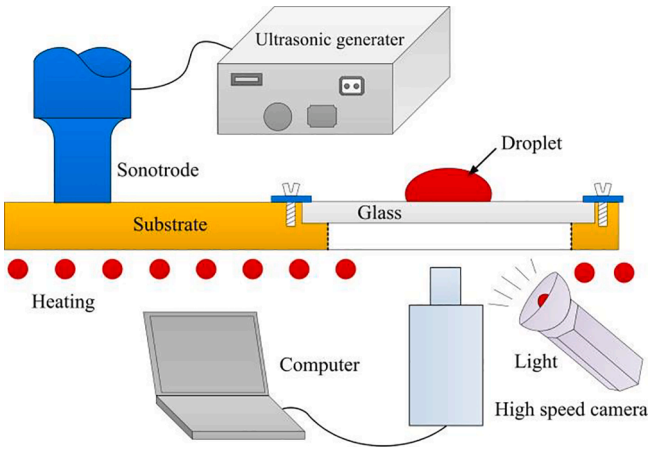

Fig. 1. Schematic of the cavitation recording experiment.

Thus, the details of the nucleation, growth, and collapse of a single bubble are difficult to acquire. Third, the liquid metal used during synchrotron X-ray imaging technology has to be thin enough to induce good penetration of the X-ray. This particular experimental setup makes it different from the actual wetting/welding process.

High-speed photography can obtain high quality images at extremely high frame rates; thus, it is a promising method that can be used to record changes in cavitation bubbles over extremely short times [40,41]. Moreover, high-speed photography can record the cavitation characteristics on a specific surface, thus providing a clear description of the evolution behavior of cavitation bubbles. During ultrasonic-assisted soldering, the cavitation bubbles that collapse near the solid substrate can help remove the oxide layer [42–44]. If we put a solder droplet on a transparent glass, the specular reflection at the solder/glass interface allows us to observe the cavitation characteristics at the solid/liquid wetting interface. This process can perfectly reveal the wetting mechanism caused by the cavitation bubbles.

In the current work, we aimed to reveal the wetting mechanism by observing the cavitation bubble characteristics at the solder/substrate interface through high-speed photography during the droplet spreading process. The cavitation characteristics and variation process were studied and then correlated by acoustic pressure simulation. This work provides a detailed analysis of the wetting mechanism of liquid solders on a substrate during ultrasonic-assisted spreading. Thus, the findings may be used as a reliable reference for future research on the mechanism of ultrasonic melt processing and cavitation.

2. Experimental

Pure Al sheet measuring 90 mm × 40 mm × 3 mm was selected as the substrate. A pure Sn droplet with a diameter of approximately 6 mm was placed on the pure Al substrate before ultrasonication. A UPM-U-P1010A01 ultrasonic system with a frequency of 20 kHz (here, T refers to one acoustic period, which is 50 μs) and maximum rated power (Pm) of 1000 W was used. The system was operated under three output power modes: 1/3 Pm (Mode I), 2/3 Pm (Mode II), and Pm (Mode III). The sonotrode was kept in place against the substrate by its own weight. The pure Sn droplet was heated to 250 °C, after which the ultrasonic vibration was turned on. The ultrasonic time was set to 1 s. After spreading, the microstructure at the Sn/substrate interface was studied on a Zeiss scanning electron microscope (SEM) to investigate the wetting condition.

The cavitation characteristics during the spreading of the pure Sn droplet were studied to reveal the wetting mechanism. Therein, a square groove was machined at the right side of the substrate, and a transient glass slide was placed in this groove to observe the cavitation characteristics (Fig. 1). The pure Sn droplet with the same diameter was manually placed at the center of the glass. During the spreading of the Sn droplet, the cavitation characteristics were recorded with a high-speed camera (Phantom VEO 719L) equipped with a macro lens (CANON MP-E 65 mm f/2.8 1–5x). The camera was assembled below the glass slide to observe the droplet spreading and the resulting cavitation bubbles. A high-intensity light source was used to provide sufficient light to the observation region. Images were obtained at an acquisition rate of 5000 fps (1280 × 800 pixels) for general spreading process.

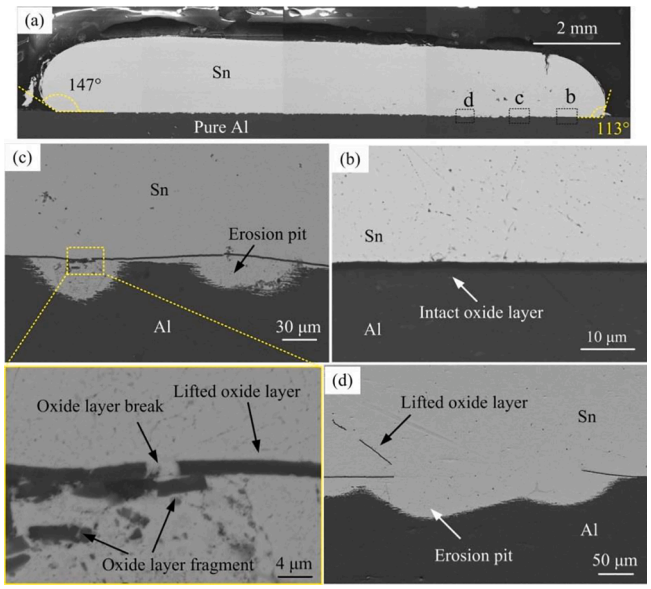

Fig. 2. Spreading of pure Sn droplet on pure Al substrate: (a) cross-section of the Sn droplet after spreading, (b) region b, (c) region c, and (d) region d.

3. Results

3.1. Spreading of Sn droplet on a nonwetted Al substrate

Fig. 2a shows the cross section of Sn droplet on the Al substrate after ultrasonic-assisted spreading for 1 s. The ultrasonic successfully realizes the spreading of the Sn droplet on the aluminum plate. The contacting angles at the spreading fronts are 113° and 147°, indicating that the spreading is realized under a nonwetting condition. The spreading radius also reached 13 mm within 1 s, showing an extremely fast spreading velocity. The rapid spreading behavior of the solder droplet on nonwetting substrate under ultrasonication was introduced in detail in one of our studies [45], but was not discussed in detail here. Fig. 2b shows the microstructure at the solder/substrate interface at the spreading front, and as can be seen, the oxide layer remains intact. Such a result indicates that no cavitation occurs at the spreading [46] front.

Meanwhile, Fig. 2c shows the interface adjacent to the spreading front. As shown in the figure, discontinuous erosion pits are observed. The oxide layer floats above the erosion pits due to the undermining. Small cracks are observed above the erosion pit (as shown in the enlarged figure). Fig. 2d shows the microstructure near the spreading center and indicates the presence of continuous erosion pits. Furthermore, the oxide layer is obviously broken, and discontinuous oxide fragments float above the erosion pits. However, the oxide layer is incompletely removed due to the relatively short ultrasonic time.

The removal of oxide layer at the interface mainly depends on the cavitation of the solder. Thus, studying the cavitation at the wetting interface is extremely important in revealing how the wetting process occurs. The cavitation at the wetting interface was studied by using high-speed photography, and numerical simulations were conducted in the follow-up work.

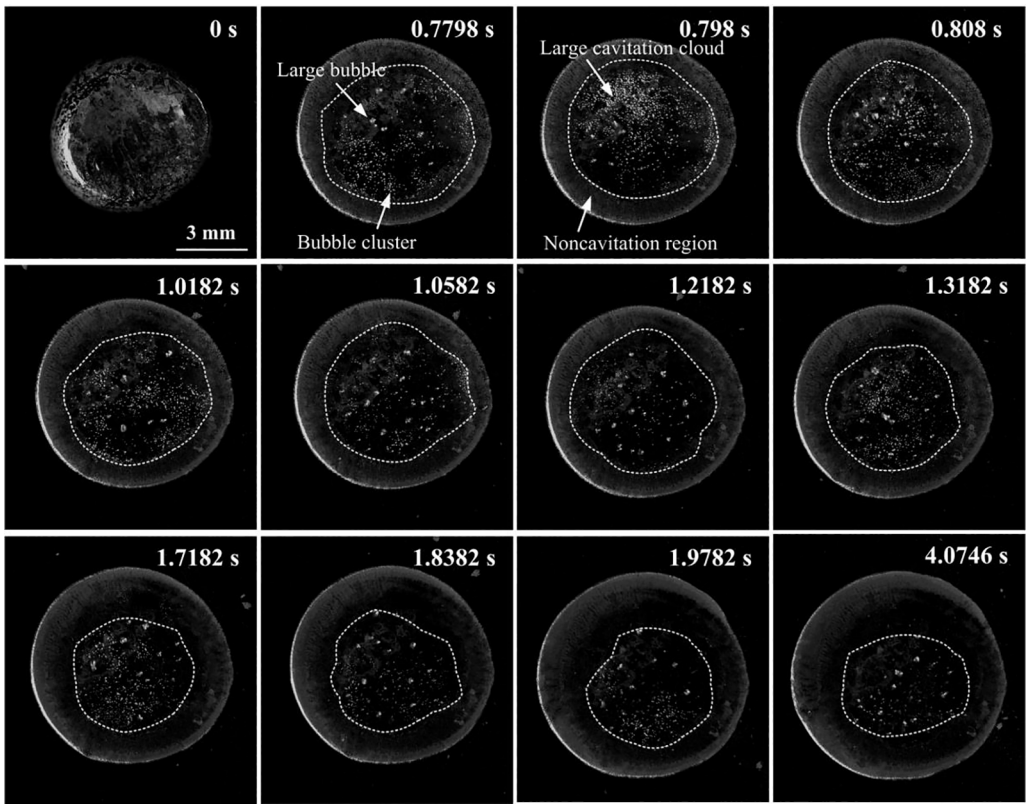

Fig. 3. Cavitation characteristics at different times during the ultrasonic-induced spreading of pure Sn droplet.

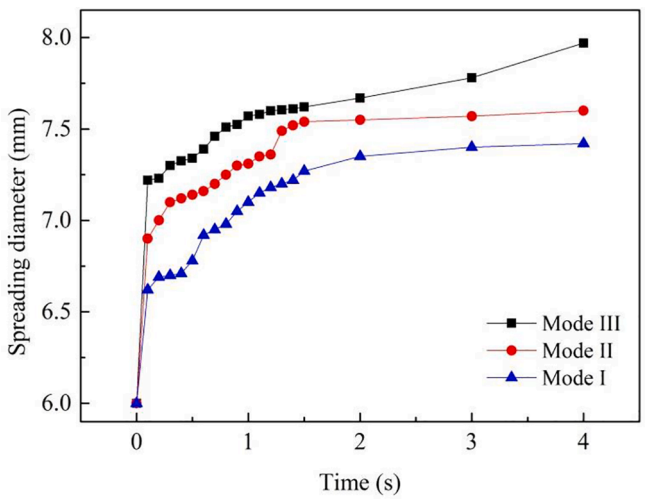

Fig. 4. Droplet diameters during spreading under different ultrasonic power modes.

3.2. Cavitation characteristics at the wetting interface during spreading

Fig. 3 shows the process of cavitation evolution during ultrasonic-assisted spreading. Here, the ultrasonication power was Mode II, and the images were obtained at an acquisition rate of 5000 fps. The Sn droplet presents a circular shape after melting on the glass at 0 s. The relative white region is the oxide layer on Sn droplet. This oxide layer can block the view and prevent the observation of the cavitation bubble in the Sn droplet. A period longer than 0.5 s is needed to remove such oxide layer. Cavitation bubbles can only be observed after the oxide layer is completely removed.

Numerous tiny cavitation bubbles and several large bubbles are also observed at 0.7798 s. These tiny bubbles form a cavitation cluster. A large cavitation cloud is observed at 0.798 s, along with some large bubbles. The bubble density gradually decreases with the increase in time, and large and tiny bubbles are observed during the whole time. The cavitation intensity remarkably decreases after 4 s, after which only a small number of cavitation bubbles are observed at 4.0746 s. The continuous generation and collapse of these cavitation bubbles produce a series of extreme and distinct phenomena in which the oxide film on the substrate is removed and the wetting of the solder to substrate is realized. Fig. 3 shows that the spreading area of the droplets gradually increases, whereas the cavitation intensity decreases with time during the spreading process of the droplet.

Meanwhile, Fig. 4 shows the spreading diameters of the droplets at different times using different ultrasonic powers. As can be seen, all the droplets spread rapidly during the first 0.1 s of ultrasonication, and the spreading velocity gradually decreases with time. Slow spreading is observed after 1 s, while large spreading diameters are obtained at high ultrasonication powers. A spreading diameter of 6.62 mm is achieved at 0.1 s at Mode I, and this value increases to 7.22 mm at Mode III. Similarly, a spreading diameter of 7.42 mm is achieved after 4 s of ultrasonication, and this value increases to 7.97 mm when using ultrasonication power of Mode III. Furthermore, Fig. 3 shows that high bubble densities can be obtained at the early-spreading stage. Combining the data shown in Figs. 3 and 4, we can conclude that fast solder spreading is always accompanied by strong cavitation effects and that droplets spread slowly under decreased cavitation intensities. This phenomenon can be attributed to a decrease in acoustic pressure at the late-spreading stage, which is discussed in the following sections.

Fig. 5 shows the cavitation characteristics of the droplet as it spreads under varied ultrasonic powers, resulting in different spreading speeds that, in turn, lead to different liquid thicknesses. Different acoustic pressures and cavitation characteristics can be obtained under such conditions. As shown in Fig. 5a, a few single bubbles are observed at 1 s, and the size of these bubbles is extremely small at Mode I. The bubble

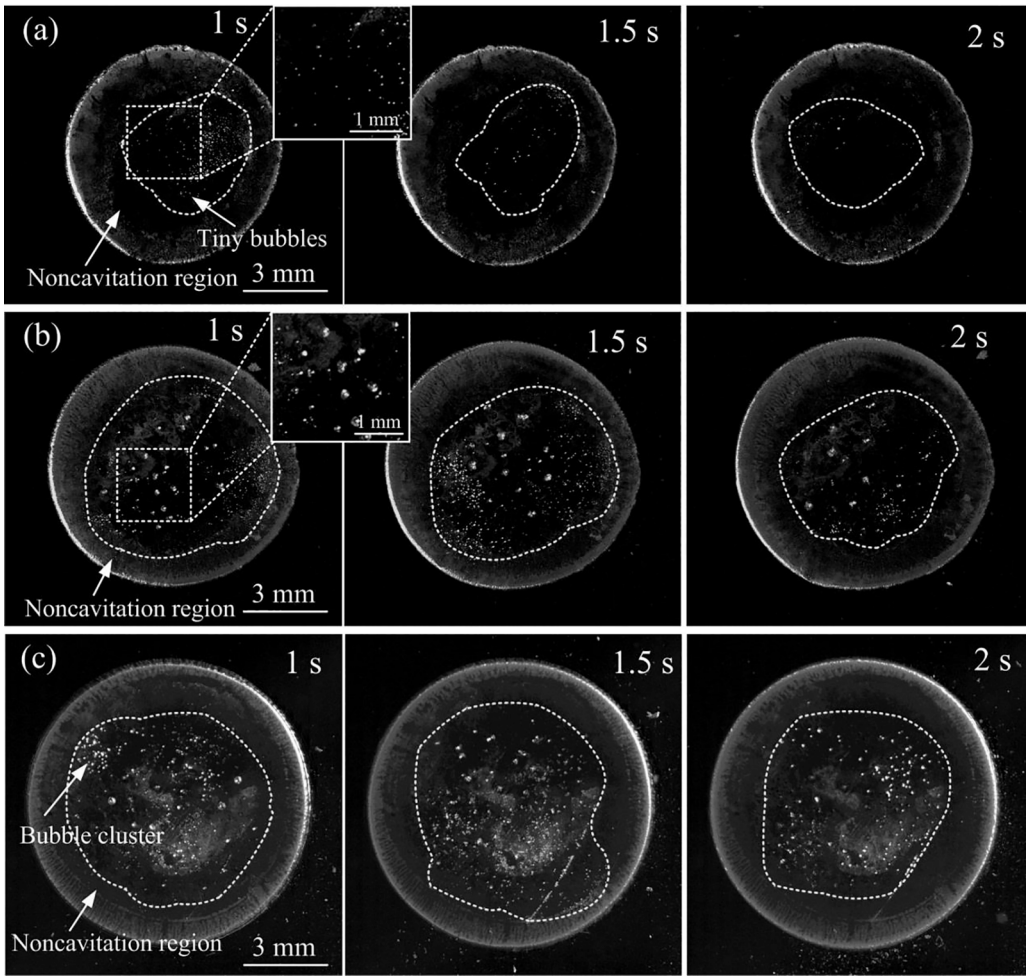

Fig. 5. Cavitation characteristics under different ultrasonic power modes: (a) I, (b) II, and (c) III.

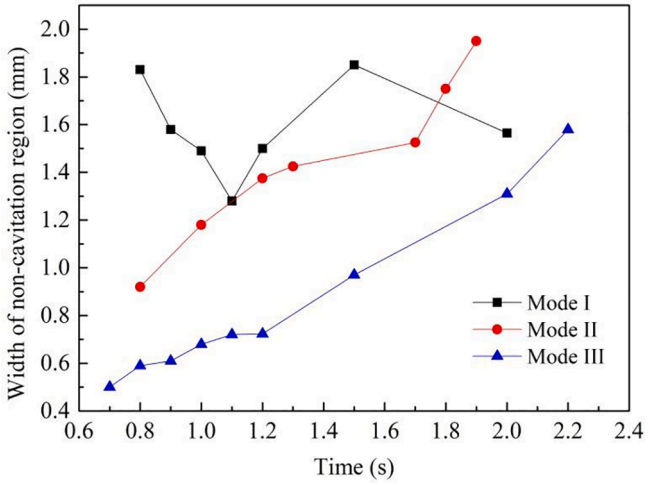

Fig. 6. Widths of noncavitation regions under different ultrasonic power modes.

density gradually decreases with the increase in time. Only several bubbles are obtained at 1.5 and 2 s. Fig. 5b shows the cavitation characteristic using Mode II. Compared with those in Mode I, cavitation bubbles are larger in size and greater in number after using Mode II. Accordingly, more bubbles than those observed at Modes I and II are generated at the glass/droplet interface when the ultrasonic power is Mode III. A bubble cluster is also observed at 1 s. Similar to those observed using Modes I and II, the bubble density gradually decreases with the increase in time. The results in Fig. 5 demonstrate that increasing the ultrasonic power remarkably enhances the cavitation intensity.

A noncavitation region can be observed at the spreading front during the entire spreading process, as shown in Fig. 3. The contour recognition of the cavitation and noncavitation regions was manually marked based on the droplet morphology observed by the high-speed camera. The noncavitation region can be observed under all power modes (Fig. 5). The results shown in Figs. 3 and 5 reveal that the widths of the noncavitation regions gradually increase with the increase in the size of the spreading area. Meanwhile, Fig. 6 shows the widths of the noncavitation regions under different ultrasonic powers. Three main conclusions can be obtained. First, the noncavitation region has a large width when using low ultrasonic powers; however, this decreases with the increase in ultrasonic power. Second, the width of the noncavitation region gradually increases with time. Third, the widths of the noncavitation region under ultrasonication of Mode I show unstable variation. As reported, the oxide layer removal mainly depends on the collapse of cavitation bubbles during ultrasonic-assisted spreading. Therefore, the oxide layer on the substrate cannot be eliminated at the noncavitation region, as shown in Fig. 2.

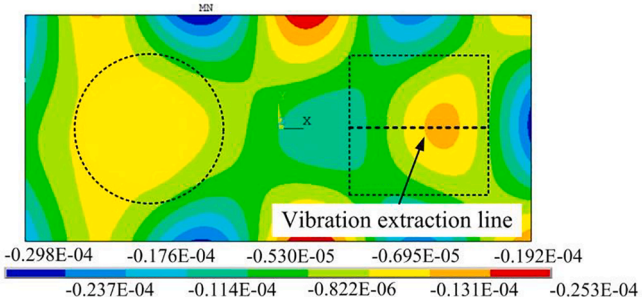

Fig. 7. Vibration conditions on the surface of pure Al using Mode I (unit m).

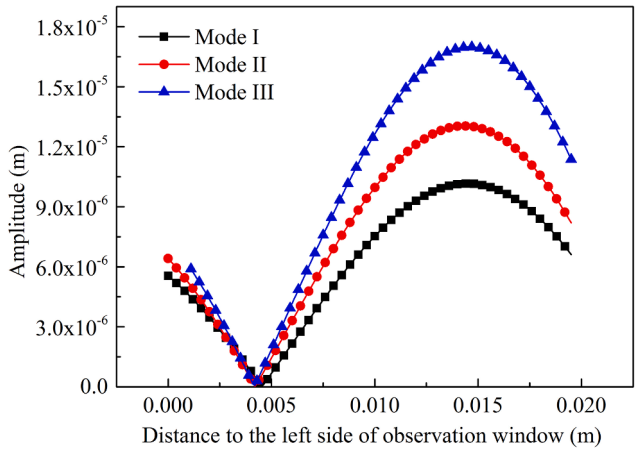

Fig. 8. Amplitudes on the substrate surface under different ultrasonic power modes.

4. Discussion

4.1. Vibration and acoustic pressure simulation

The cavitation intensity is closely related to the vibration on the substrate surface [39]. Specifically, stronger vibrations on a substrate surface lead to stronger cavitation effects in the liquid. Here, we simulated the vibrations on the substrate surface by ANSYS. A solid model is established by ANSYS APDL 15.0 and meshed by the Brick 20 Node 186 unit at 1 mm intervals. The same parameters applied to the cavitation recording experiment were used during the simulation. The ultrasonic vibration was applied on the left side of the substrate (marked by the dotted circle). The corners of the substrate remained fixed. The calculation was convergent during the calculation. Fig. 7 shows the surface vibration characteristics of the pure aluminum substrate at Mode I (i.e., Harmonic analysis) and shows the stable vibration condition after applying the ultrasonic vibration. Different colors represent various vibration amplitudes. The vibration on the substrate surface is distributed symmetrically around the X-axis. The weakest vibrations are experienced by the area near the sonotrode because this area tightly contacts the latter. In comparison, the strongest vibrations are experienced by the sheet edge, which has less constraint. The vibration amplitudes along the dotted line are extracted and analyzed because the liquid droplet spreads along this line.

Fig. 8 shows the amplitudes along the vibration extraction line using different ultrasonic powers. As can be seen, the amplitude first decreases, increases, and further decreases from the left to the right side. The maximum amplitude of 10.2 μm is obtained when using Mode I. Higher ultrasonic power results in stronger vibration. The maximum amplitude increases to 13.0 and 17.0 μm when using Modes II and III. At the same time, a region with extremely low vibration amplitude is found at 4.6 mm from the left side of the observation window. The low vibration amplitude in this region does not produce low acoustic pressure and low bubble density. Details of this phenomenon were discussed in one of our studies [47].

A geometric model with a diameter of 20 mm × 10 mm was established on GAMBIT software prior to the simulation of acoustic pressure. The model was then meshed with a grid width of 0.1 mm, and the boundary conditions were defined. As marked in Fig. 9a, the left and right surfaces of the model were defined as walls. The lower surface and upper surface were defined as a vibratory wall and a pressure outlet, respectively. The model was loaded in FLUENT for calculation. Vibrations that were extracted from the results shown in Fig. 8 were applied to the bottom surface of the model during the calculations. The parameters applied during the calculation are as follows: surface tension of pure Sn, 0.556 N/m; density of pure Sn, 7.31 g/cm^3; viscosity of pure Sn, 2.64 × 10^{-3} Pa•s; contact angle between Sn and substrates, 130°; and surface roughness of the substrate, 0.0015 mm. The droplet was assumed to have a semicircular morphology with a diameter of 6 mm, as shown in Fig. 9b. In the figure, the atmospheric environment is in red and the Sn liquid is in blue.

4.2. Droplet spreading process

Fig. 10 shows the spreading morphology and acoustic pressure fields of the droplet within 60 T. Here, the ultrasonication power is Mode II. At 1 T, the droplet just spreads, and its initial semicircular morphology is retained (Fig. 10a). The internal acoustic pressure of the droplet has a positive value, and the maximum value of 1.60 × 10^6 Pa is obtained in the droplet center (Fig. 10b). Fig. 10c shows the spreading morphology at 10 T. The droplet spreads to a radius of approximately 7.1 mm. Fig. 10d shows the acoustic pressure field at 10 T. Compared with that shown in Fig. 10b, the droplet spreading leads to thinner liquid, which then decreases the acoustic pressure to 1.43 × 10^6 Pa. The droplet shows obvious spreading at 30 T, and the spreading diameter increases to 8.1

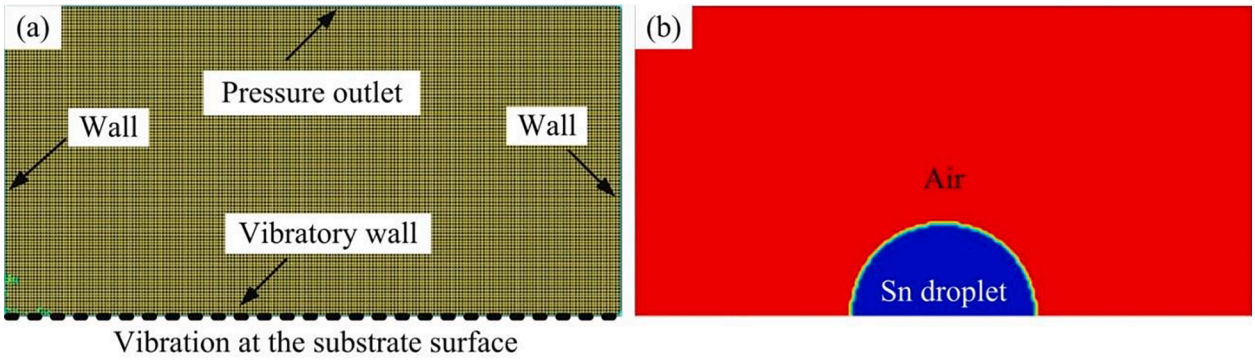

Fig. 9. Simulation system: (a) boundary conditions and (b) initial state.

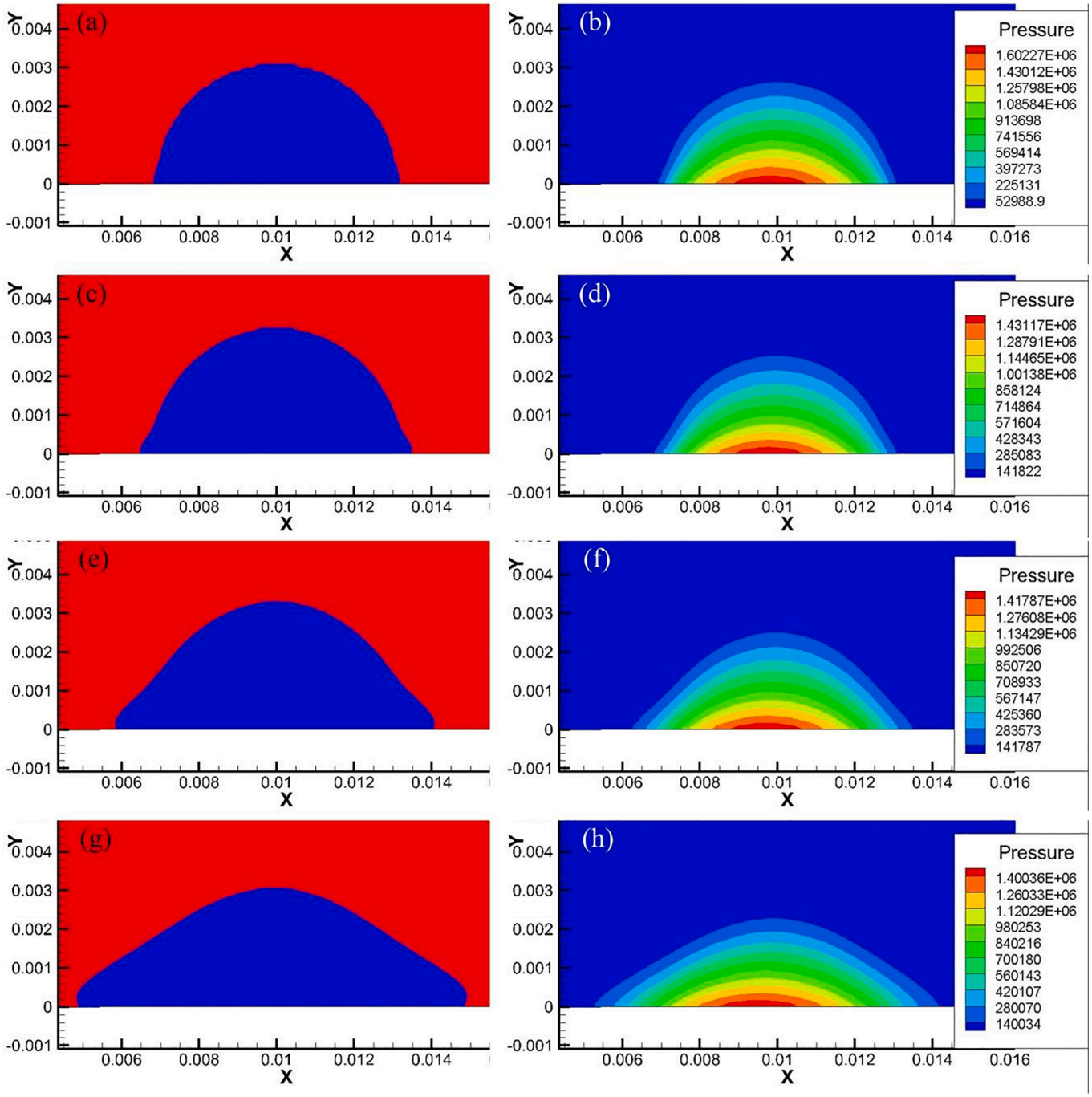

Fig. 10. Droplet morphology and pressure field at 1 T (a and b, respectively), 10 T (c and d, respectively), 30 T (e and f, respectively), 60 T (g and h, respectively) at Mode II.

mm (Fig. 10e). The acoustic pressure inside the droplet decreases to 1.42×10^6 Pa with its further spread (Fig. 10f). The spreading diameter increases to approximately 10 mm at 60 T (Fig. 10g), after which the pressure at the droplet center decreases to 1.40×10^6 Pa (Fig. 10h).

Some important information can be obtained from Fig. 10. First, the acoustic pressure gradually decreases with the spreading of the droplet. This phenomenon corresponds well with the results obtained in Fig. 2, that is, the cavitation intensity decreases gradually with the spreading of the droplet. The decreased acoustic pressure due to the spreading of the droplet well explains the phenomenon in which the width of the non-cavitation region gradually increases with time. The acoustic pressure at the late spreading stage is lower than that at the initial spreading stage due to thinner liquid. Accordingly, the acoustic pressures in more regions are below the cavitation threshold after the droplet spreads. Second, the peak acoustic pressure is obtained at the droplet center and gradually decreases outward from this region. This pressure gradient facilitates the outward flow of the liquid and realizes the spreading process of the droplet [45].

Fig. 11 shows the acoustic pressure near the solder/substrate interface (0.01, 0.0001) within 3 T, using different ultrasonic powers. The result shows that higher acoustic pressure can be obtained when using higher ultrasonic powers. In particular, the maximum pressure is 2.38 MPa when using Mode I, and this value increases to 3.86 and 5.45 MPa when Modes II and III are used, respectively. Higher acoustic pressure always results in stronger cavitation. Thus, the acoustic pressure variation in Fig. 11 corresponds well with the results in Fig. 5, that is, the

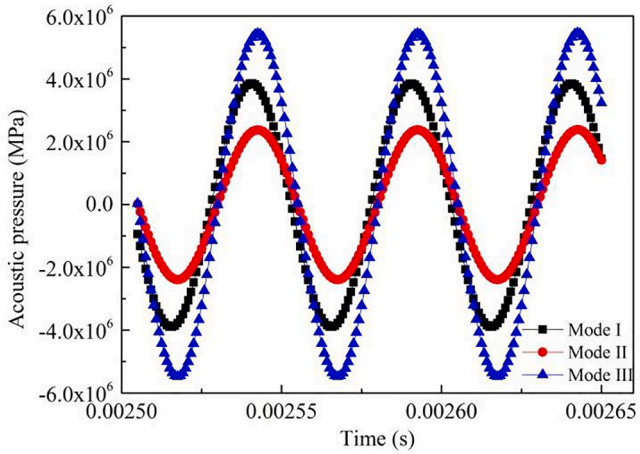

Fig. 11. Acoustic pressure within 3 T using different ultrasonic powers.

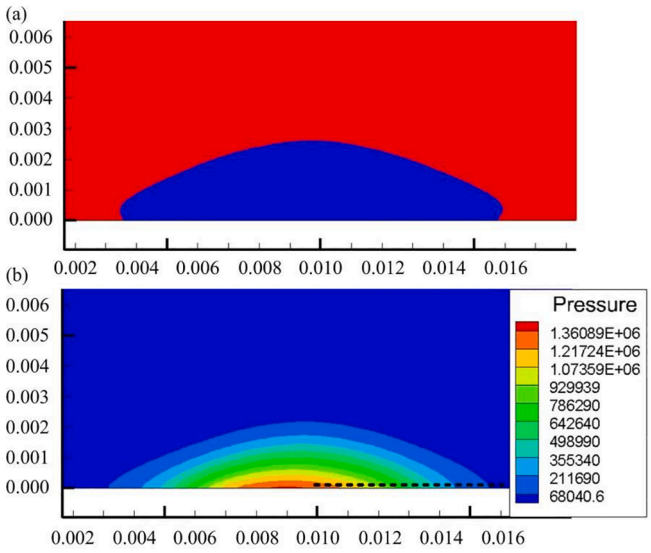

Fig. 12. Spreading morphology (a) and acoustic pressure field (b) at 1000 T.

cavitation intensity increases when using higher ultrasonic power. The phenomenon in which the widths of the noncavitation regions decrease with the increase in ultrasonic power can be explained by the acoustic pressure results. As introduced in Fig. 11, higher acoustic pressure can be obtained at the same thick liquid when using higher ultrasonic power. This result indicates that more region of the liquid reaches the cavitation threshold, resulting in cavitation. Thus, narrower noncavitation regions can be obtained when using higher ultrasonic power.

4.3. Noncavitation at the spreading front

Figs. 5 and 6 show that a noncavitation region exists at the spreading front during spreading. A previous study has reported that cavitation is closely influenced by the acoustic pressure inside a liquid [46]. A certain pressure inside the liquid, known as the cavitation threshold, must be overcome to initiate cavitation. In this study, the acoustic pressure from the droplet center to its spreading front was extracted and analyzed to investigate the phenomenon of noncavitation. Fig. 12 shows the spreading morphology and acoustic pressure field inside the droplet at 1000 T. As can be seen, the droplet shows obvious spreading at the three-phase interface (Fig. 12a), and the width of the noncavitation region at this point is 0.7 mm. Fig. 12b illustrates that the acoustic pressure inside the solder droplet has a positive value and that the

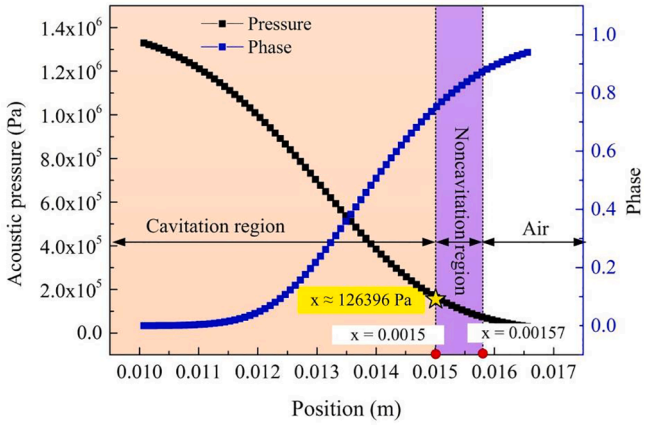

Fig. 13. Phase and pressure at the extraction points at 1000 T.

pressure gradually decreases from the center of the droplet to its exterior.

Fig. 13 shows the acoustic pressure and phase extracted from the droplet center to the spreading front (marked by the dotted line in Fig. 12b). As shown in Fig. 13, pressure gradually decreases from the droplet center to its spreading front and becomes stable in the atmosphere. The air phase ratio is 0 in the droplet and 1 in the atmosphere. These findings, combined with the spreading morphology and data in Figs. 12a and 13, reveal that the spreading front is located at approximately x = 15.7 mm. In addition, the width of the noncavitation zone at the droplet front is approximately 0.7 mm. Therefore, x = 15.0 mm must be the edge of the cavitation zone, that is, the acoustic pressure at this point can be assumed to be the cavitation threshold of the pure Sn. Therefore, the sound pressure at x = 15.0 mm is 126,396 Pa.

To verify the cavitation threshold, we recorded the widths of the noncavitation regions and compared them with the simulation results. Fig. 14a shows the experimental and simulation results of the noncavitation regions at different spreading diameters. The data obtained by simulation corresponds well with those obtained by experiment, thus proving that the proposed method has high accuracy and credibility. In particular, the widths of the noncavitation regions show a linear relationship with the spreading diameter of the droplet. During spreading, the droplet can be divided into a cavitation region at its center and a noncavitation region at its surface. The acoustic pressure at the interface of the two regions is the cavitation threshold, which is 126, 396 Pa.

In addition, Fig. 14b–14e show the spreading morphologies obtained by simulation and experiment. During simulation, a noncavitation region with a width of 0.6 mm emerged at the spreading front when the droplet spread to 7.5 mm. This result corresponds well with the cavitation characteristic recorded by the high-speed camera, indicating the presence of a 0.62 mm-wide noncavitation region (Fig. 14b). Similarly, a 1 mm-wide noncavitation width is observed in the simulation when the droplet spread to 9.3 mm. The experiment results reveal that the noncavitation region is approximately 0.92 mm at this moment (Fig. 14c). When the droplets spread to 11.9 and 15.3 mm, the noncavitation regions obtained through simulation are also well proven by the experiment results (Fig. 14d and e, respectively).

4.4. Bubble dynamics calculation

Fig. 15 shows the acoustic pressures at the point (0.01, 0.0001) near the solder/substrate interface in the droplet within 5 T at different spreading stages. As can be seen, the acoustic pressure at different spreading stages all presents sine-like morphologies. We fitted the acoustic pressure variation curves using Origin software. The acoustic pressure equations inside different channels are listed as follows:

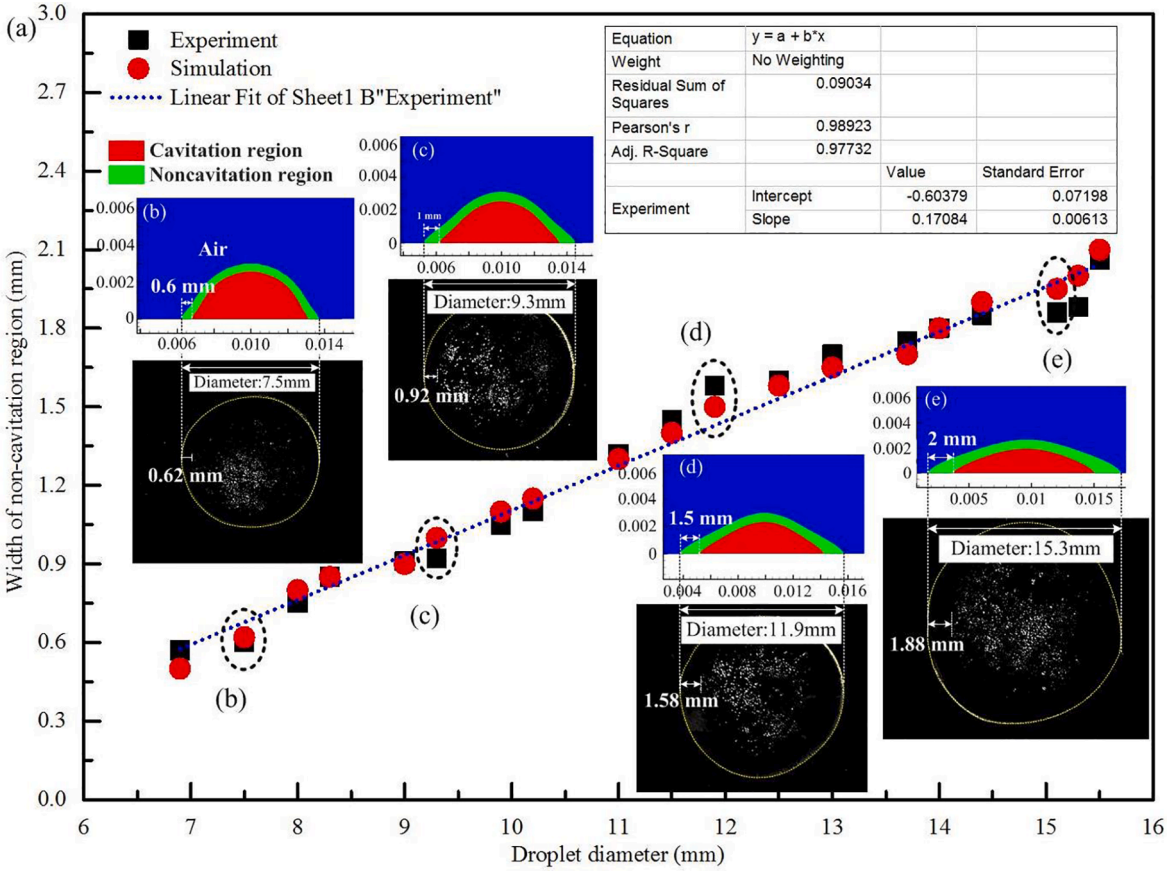

Fig. 14. Noncavitation region at the spreading front obtained through simulation and experiment at various spreading diameters of (a) 7.5 mm, (b) 9.3 mm, (c) 11.9 mm, and (d) 15.3 mm.

$$P = -7782.14 + (3.86 \times 10^{6}) \times \sin\{2\pi \times 20,000\left[x - \left(2.80\times10^{-5}\right)\right]\}60 - 65T \quad (1)$$

$$P = -11796.40 + (3.47 \times 10^{6}) \times \sin\{2\pi \times 20,000\left[x - \left(2.80\times10^{-5}\right)\right]\}95 - 100T \quad (2)$$

The acoustic pressure equations at different times are expressed as

$$P = P_x + P_y \times sin[2\pi f(x - x_0)], \quad (3)$$

where P is the acoustic pressure inside the solder (whose unit is Pa), P_y is the amplitude of the pressure variation, P_x is the offset of the pressure equation, f is the frequency, and x_0 is the initial phase of the fitted curve. The result shows that f is consistent with that of the applied ultrasonic, which is 20 kHz.

As indicated in Eqs. (1) and (2), the maximum acoustic pressure during 55–60 T is 3.86 MPa. The acoustic pressure gradually decreases with the spreading of the liquid droplet, while the maximum pressure during 95–100 T is 3.47 MPa. The cavitation intensity is proportional to the acoustic pressure inside the solder, such that a higher acoustic pressure always results in stronger cavitation. Thus, more cavitation bubbles can be observed during the initial spreading stage, as shown in Fig. 2.

Next, we calculated the cavitation bubble dynamics to investigate the wetting mechanism of the ultrasonic soldering using a modified Rayleigh–Plesset (R–P) equation:

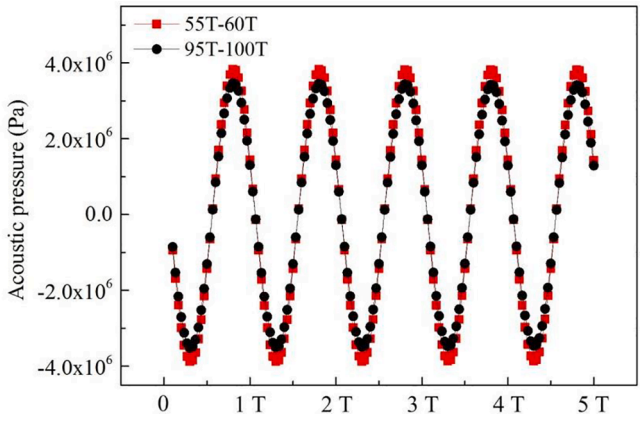

Fig. 15. Acoustic pressure within 5 T at different spreading stages.

The temperature generated when a cavitation bubble collapses can be calculated with Equation (6):

$$T_{collapse} = T_0 \left(\frac{R_0}{R}\right)^{3(n-1)} \tag{6}$$

where R_0 is the initial diameter of the cavitation bubble; P_0 is the hydrostatic pressure of the liquid metal; $\frac{2\sigma}{R_0}$ is the surface tension of the bubble; μ is the viscosity coefficient of the liquid metal, which is assumed to be 0.0013; and n is the exponent reflecting the thermodynamic state of the cavitation bubble. Suppose that the gas inside the cavitation bubble is air, the $n = 1.4$. P_A is the acoustic pressure variation given in Eqs. (1) and (2). Given that Eq. (4) is a second-order ordinary differential equation, obtaining an analytical solution is difficult. Thus, we used the fourth Runge–Kutta method to obtain a numerical solution.

In this section, the bubble dynamics and velocity of the bubble wall at different spreading stages were calculated, along with the pressure and temperature generated when the cavitation bubble collapses. The

$$R\left(\frac{d^2R}{dt^2}\right)+\frac{3}{2}\left(\frac{dR}{dt}\right)^2 = \frac{1}{\rho}\left[\left(P_0+\frac{2\sigma}{R_0}\right)\left(\frac{R_0}{R}\right)^{3n} - P_A - P_0 - \frac{2\sigma}{R}\right] - \frac{4\mu}{\rho R}\frac{dR}{dt} + \frac{R}{\rho c}\frac{d}{dt}\left[\left(P_0+\frac{2\sigma}{R_0}\right)\left(\frac{R_0}{R}\right)^{3n} - P_A\right] \tag{4}$$

The pressure generated when a cavitation bubble collapses can be calculated using Eq. (5):

$$P_{collapse} = \left(P_0+\frac{2\sigma}{R_0}\right)\times\left(\frac{R_0}{R}\right)^{3n} - \frac{2\sigma}{R_0} - \frac{4\mu}{R}\left(\frac{dR}{dt}\right). \tag{5}$$

nucleation diameter of the cavitation bubble was assumed to be 20 μm. Fig. 16a shows the bubble dynamics within 3 T at different spreading stages. The black line represents the bubble during 55–60 T, and the red line represents the bubble during 95–100 T. The results show that all the cavitation bubbles oscillate approximately 0.5 T after nucleation. The cavitation bubbles also grow rapidly. In particular, the bubble formed during the 55–60 T rapidly grows to 61.8 times of its initial size within

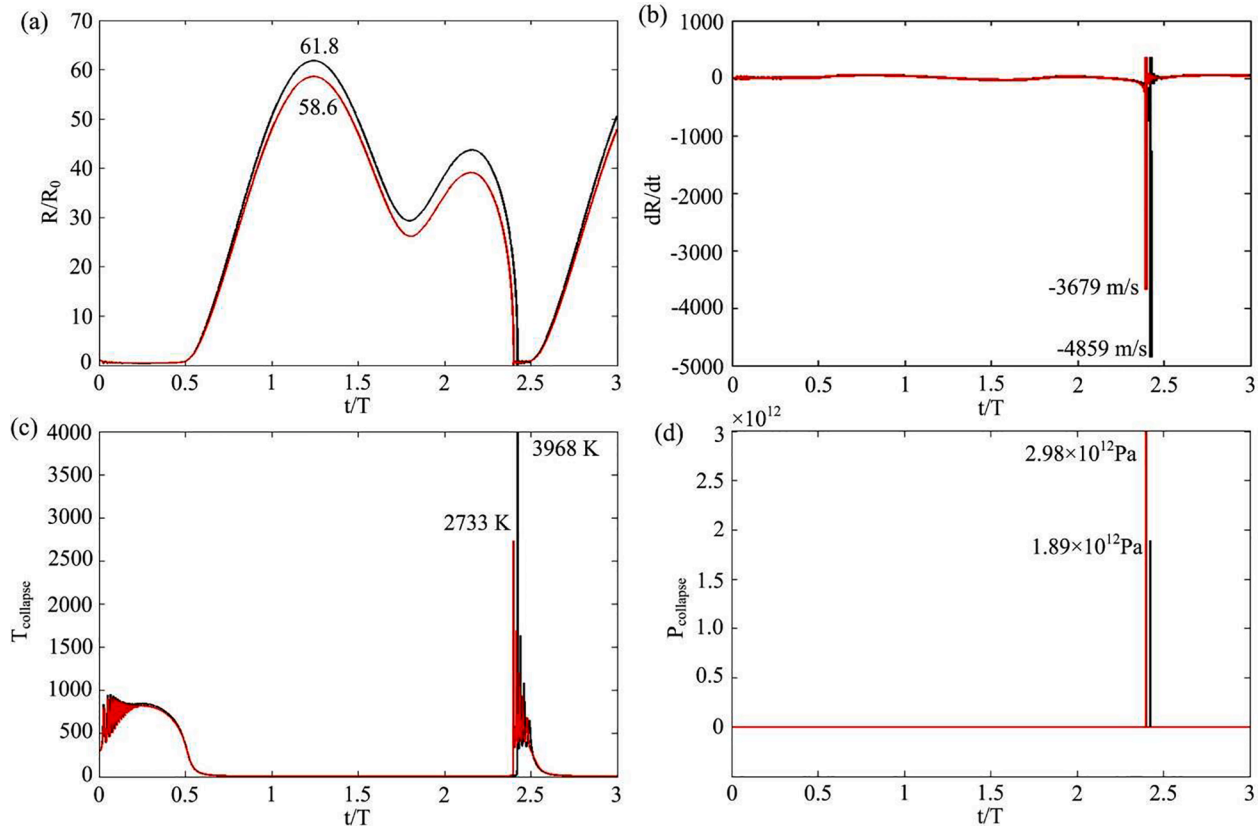

Fig. 16. Bubble dynamics: (a) R/R_0 within three acoustic periods, (b) collapse velocities of bubble wall, (c) temperatures, and (d) pressures of bubble collapse.

0.8 T. At the same time, the acoustic pressure gradually decreases with the spreading of the droplet, resulting in slower bubble growth velocity and smaller bubble diameter. In comparison, the bubble formed within 95–100 T only grows to 58.6 times of its initial size. Similarly, all the cavitation bubbles formed during the three stages do not collapse within 1 T, and they all have lives of approximately 2.5 T before the first collapse.

When ultrasonic soldering Al alloys, the wetting is realized only when the oxide layer of substrate is removed. The removal of the oxide layer involves several processes. The first process is mechanical shock, which is mainly caused by shock wave or microjet formed by bubble collapse. Fig. 16b shows the velocities of the bubble wall when they collapse. As can be seen, the bubble formed during the 95–100 T has a collapse wall velocity of 3679 m/s, which increases with the increase in the acoustic pressure of liquid. The bubble has a collapse velocity of 4859 m/s when it formed during 55–60 T. Such large velocities of the bubble wall can lead to shock wave with large energy and pressure, which, in turn, can break the oxide layer directly [40]. The second mechanical shock format when removing the oxide layer is the microjet, which occurs when the cavitation bubble collapses near the solid wall. The microjet can have a velocity higher than 100 m/s, which can directly pierce the oxide layer.

Fig. 16c shows the temperature generated when the cavitation bubble collapses. The result shows that the collapse of the cavitation bubble produces a high temperature of 3968 K when it formed during 55–60 T. Such high temperature can directly melt the oxide layer or make it extremely soft. The collapse temperature, which changes by altering the acoustic pressure, decreases to 2733 K when it forms and collapses during 95–100 T. The high temperature during the collapse of the bubble has been reported by some researchers [17,20], and high collapse temperatures are obtained in all the references. Another particular phenomenon caused by bubble collapse is high pressure. Fig. 16d shows the pressure generated when the cavitation bubble collapses. The cavitation bubble formed during 55–60 T results in an extremely high pressure of 1.89×10^{12} Pa, under which the oxide layer and the substrate can be directly broken. The pressure further increases to 2.98×10^{12} Pa when the cavitation bubble collapses during 95–100 T.

Fig. 16 confirms that extreme conditions, such as high temperature and high pressure, are caused by the collapse of the cavitation bubbles. These phenomena can facilitate the easy removal of the oxide layer, erode the Al alloys rapidly during ultrasonic soldering, and account for the chemical reactions when ultrasonic soldering some hard-to-wet materials, such as ceramics and sapphires [48].

5. Conclusions

1. Ultrasonication realizes the spreading of pure Sn droplet on pure Al substrate at a nonwetting condition. The oxide layer of the substrate at the spreading fronts is not removed because the cavitation cannot occur.
2. The cavitation intensity at the droplet/substrate interface gradually decreases with the spreading of the droplet. In addition, higher ultrasonic power results in higher cavitation intensity. This condition is explained by the acoustic pressure simulation of the solder.
3. A noncavitation region can be observed at the spreading front, because the acoustic pressure is lower than the cavitation threshold of 1.26 MPa when the temperature is 250 °C. The width of the noncavitation region gradually increases with the spreading process. Higher ultrasonic power reduces the width of the noncavitation region.
4. The wetting mechanism caused by the collapse of the cavitation bubble is explained from the viewpoint of bubble dynamics calculation. The high velocity of the bubble wall, high pressure, and high temperature are all generated when the cavitation bubbles collapse.

CRediT authorship contribution statement

Zhengwei Li: Writing – original draft, Investigation, Methodology, Software. **Zhiwu Xu:** Methodology. **Peng He:** Supervision. **Zhongwei Ma:** Investigation. **Shu Chen:** Software. **Jiuchun Yan:** Supervision.

Declaration of Competing Interest

The authors declare that they have no known competing financial interests or personal relationships that could have appeared to influence the work reported in this paper.

Acknowledgement

This project was supported by the National Natural Science Foundation of China (No. 51574099).

Data availability

The data that support the findings of this study are available from the corresponding author upon reasonable request.

References

[1] C. Peng, S. Tian, G. Li, M.C. Sukop, Simulation of laser-produced single cavitation bubbles with hybrid thermal Lattice Boltzmann method, Int. J. Heat. Mass. Trans. 149 (2020), 119136.
[2] C.E.H. Tonry, G. Djambazov, A. Dybalska, W.D. Griffiths, C. Beckwith, V. Bojarevics, K.A. Pericleous, Acoustic resonance for contactless ultrasonic cavitation in alloy melts, Ultrason. Sonochem. 63 (2020), 104959.
[3] K. Graff, Marcosonics in industry: ultrasonic soldering, Ultrasonics 15 (1977) 75–81.
[4] X. Chen, J. Yan, F. Gao, J. Wei, Z. Xu, G. Fan, Interaction behaviors at the interface between liquid Al–Si and solid Ti–6Al–4V in ultrasonic-assisted brazing in air, Ultrason. Sonochem. 20 (2013) 144–154.
[5] L. Ma, Z. Xu, K. Zheng, J. Yan, S. Yang, Vibration characteristics of aluminum surface subjected to ultrasonic waves and their effect on wetting behavior of solder droplets, Ultrasonics 54 (2014) 929–937.
[6] Y. Li, W. Zhao, X. Leng, Q. Fu, L. Wang, J. Yan. Microstructure evolution and mechanical properties of ultrasonic-assisted soldering joints of 2024 aluminum alloys. Trans. Nonferrous. Met. Soc. China. 21 (2011) 1937–1943.
[7] W. Guo, X. Leng, J. Yan, Y. Tan, Ultrasonic soldering aluminum at low temperature, Weld. J. 94 (2015) 189–195.
[8] Z. Xu, Z. Li, L. Peng, J. Yan, Ultra-rapid transient liquid phase bonding of Mg alloys within 1 s in air by ultrasonic assistance, Mater. Des. 161 (2019) 72–79.
[9] Z. Xu, Z. Li, B. Chai, J. Yan, Formation of $TiAl_3$ and its reinforcing effect in TA15 alloy joint ultrasonically brazed with pure Al, J. Alloy. Compd. 815 (2020), 152493.
[10] I. Kostolný, R. Koleňák, E. Hodúlová, P. Zacková, M. Kusý, Investigation of ultrasound-assisted soldering of SiC ceramics by Zn-Al-In high-temperature solder, Weld. World. 63 (2019) 1449–1459.
[11] H. Ji, X. Cheng, M. Li, Ultrafast ultrasonic-assisted joining of bare α-alumina ceramics through reaction wetting by aluminum filler in air, J. Eur. Ceram. Soc. 36 (2016) 4339–4344.
[12] L.A. Teran, S.A. Rodŕıguez, S. Láın, S. Jung, Interaction of particles with a cavitation bubble near a solid wall, Phys. Fluid. 30 (2018), 123304.
[13] B. Boyda, S. Becker, Numerical modeling of the acoustically driven growth and collapse of a cavitation bubble near a wall, Phys. Fluid. 31 (2019), 032102.
[14] F. Dong, X. Li, L. Zhang, L. Ma, R. Li, Cavitation erosion mechanism of titanium alloy radiation rods in aluminum melt, Ultrason. Sonochem. 31 (2016) 150–156.
[15] G.I. Eskin, Ultrasonic Treatment of Molten Aluminium, Metallurgiya, Moscow, 1965.
[16] R. Oguri, K. Ando, Cavitation bubble nucleation induced by shock-bubble interaction in a gelatin gel, Phys. Fluid. 30 (2018), 051904.
[17] K.Y. Kim, K. Byun, H. Kwak, Temperature and pressure fields due to collapsing bubble under ultrasound, Chem. Eng. J. 132 (2007) 125–135.
[18] E.B. Flint, K.S. Suslick, The temperature of cavitation, Science 20 (1991) 1397–1399.
[19] Kenneth S. Suslick, David A. Hammerton, Raymond E. Cline, The sonochemical hot spot, J. Am. Chem. Soc. 108 (18) (1986) 5641–5642.
[20] Y. Shen, K. Yasui, Z. Sun, B. Mei, M. You, T. Zhu, Study on the spatial distribution of the liquid temperature near a cavitation bubble wall, Ultrason. Sonochem. 29 (2016) 394–400.
[21] K.S. Suslick. The chemical effects of ultrasound. Scientific American February 1989. 80–89.
[22] E. Brujan, Y. Matsumoto, Collapse of micrometer-sized cavitation bubbles near a rigid boundary, Microfluid. Nanofluid. 13 (2012) 957–966.

[23] X. Ma, B. Huang, X. Zhao, Y. Wang, Q. Chang, S. Qiu, X. Fu, G. Wang, Comparisons of spark-charge bubble dynamics near the elastic and rigid boundaries, Ultrason. Sonochem. 43 (2018) 80–90.
[24] Emil-Alexandru Brujan, Shock wave emission and cavitation bubble dynamics by femtosecond optical breakdown in polymer solutions, Ultrason. Sonochem. 58 (2019) 104694, https://doi.org/10.1016/j.ultsonch.2019.104694.
[25] C. Lechner, W. Lauterborn, M. Koch, R. Mettin, A new jetting mechanism for bubbles expanding and collapsing in extreme vicinity to a solid boundary, Phys. Rev. Fluids (2019), https://doi.org/10.1103/PhysRevFluids.4.021601.
[26] Zhengwei Li, Zhiwu Xu, Lin Ma, Sheng Wang, Xuesong Liu, Jiuchun Yan, Cavitation at filler metal/substrate interface during ultrasonic-assisted soldering. Part II: Cavitation erosion effect, Ultrason. Sonochem. 50 (2019) 278–288.
[27] R.L. Hunicke, Ultrasonic soldering pots for fluxless production soldering, Weld. J. 55 (3) (1976) 191–194.
[28] R.W. Gunkel, Solder aluminum joints ultrasonically, Weld. Des. Fabricat. 58 (9) (1979) 90–92.
[29] L. Zhang, D.G. Eskin, L. Katgerman, Influence of ultrasonic melt treatment on the formation of primary intermetallics and related grain refinement in aluminum alloys, J. Mater. Sci. 46 (2011) 5252–5259.
[30] G.I. Eskin, Broad prospects for commercial application of the ultrasonic (cavitation) melt treatment of light alloys, Ultrason. Sonochem. 8 (3) (2001) 319–325.
[31] H. Huang, D. Shu, Y. Fu, J. Wang, B. Sun, Synchrotron radiation X-ray imaging of cavitation bubbles in Al–Cu alloy melt, Ultrason. Sonochem. 21 (2014) 1275–1278.
[32] W.W. Xu, I. Tzanakis, P. Srirangam, W.U. Mirihanage, D.G. Eskin, A.J. Bodey, P. D. Lee, Synchrotron quantification of ultrasound cavitation and bubble dynamics in Al–10Cu melts, Ultrason. Sonochem. 31 (2016) 355–361.
[33] W. Mirihanage, W. Xu, J. Tamayo-Ariztondo, D. Eskin, M. Garcia-Fernandez, P. Srirangam, P. Lee, Synchrotron radiographic studies of ultrasonic melt processing of metal matrix nanocomposites, Mater. Lett. 164 (2016) 484–487.
[34] D.G. Eskin, I. Tzanakis, F. Wang, G.S.B. Lebon, T. Subroto, K. Pericleous, J. Mi, Fundamental studies of ultrasonic melt processing, Ultrason. Sonochem. 52 (2019) 455–467.
[35] B. Wang, D. Tan, T.L. Lee, J.C. Khong, F. Wang, D. Eskin, T. Connolley, K. Fezzaa, J. Mi, Ultrafast synchrotron X-ray imaging studies of microstructure fragmentation in solidification under ultrasound, Acta. Mater. 144 (2018) 505–515.
[36] J. Mi, D. Tan, T.L. Lee, In Situ Synchrotron X-ray study of ultrasound cavitation and its effect on solidification microstructures, Metall. Mater. Trans. B. 46 (2015) 1615–1619.
[37] Dongyue Tan, Tung Lik Lee, Jia Chuan Khong, Thomas Connolley, Kamel Fezzaa, Jiawei Mi, High-speed synchrotron X-ray imaging studies of the ultrasound shockwave and enhanced flow during metal solidification processes, Metall. Mater. Trans. A. 46 (7) (2015) 2851–2861.
[38] I. Tzanakis, W.W. Xu, G.S.B. Lebon, D.G. Eskin, K. Pericleous, P.D. Lee, In situ synchrotron radiography and spectrum analysis of transient cavitation bubbles in molten aluminium alloy, Phys. Procedia 70 (2015) 841–845.
[39] Zhengwei Li, Zhiwu Xu, Lin Ma, Sheng Wang, Xuesong Liu, Jiuchun Yan, Cavitation at filler metal/substrate interface during ultrasonic-assisted soldering Part I: cavitation characteristics, Ultrason. Sonochem. 49 (2018) 249–259.
[40] E.A. Brujan, T. Ikeda, Y. Matsumoto, On the pressure of cavitation bubbles, Exp. Therm. Fluid. Sci. 32 (5) (2008) 1188–1191.
[41] E.A. Brujan, T. Ikeda, K. Yoshinaka, Y. Matsumoto, The final stage of the collapse of a cloud of bubbles close to a rigid boundary, Ultrason. Sonochem. 18 (2011) 59–64.
[42] Emil-Alexandru Brujan, Yoichiro Matsumoto, Collapse of micrometer-sized cavitation bubbles near a rigid boundary, Microfluid Nanofluid 13 (6) (2012) 957–966.
[43] Y. Tomita, A. Shima, Mechanisms of impulsive pressure generation and damage pit formation by bubble collapse, J. Fluid. Mech 169 (-1) (1986) 535, https://doi.org/10.1017/S0022112086000745.
[44] C. Lechner, W. Lauterborn, M. Koch, et al., A new jetting mechanism for bubbles expanding and collapsing in extreme vicinity to a solid boundary, Phys. Rev. Fluids (2019), https://doi.org/10.1103/PhysRevFluids.4.021601.
[45] Z. Xu, Z. Li, L. Ma, J. Bo, J. Yan, Ultrasonic-diven spreading of liquid solder on nonwetting substrates, Weld. J. 99 (2020) 163–174.
[46] Z. Xu, Z. Li, X. Luo, S. Ji, J. Yan, Oxidation behavior at the frontier of ultrasonic-induced solder spreading on the aluminum alloy surface, Rare. Metal. Mat. Eng. 47 (11) (2018) 3426–3432.
[47] Z. Li, Z. Xu, D. Zhao, S. Chen, J. Yan, Ultrasonic cavitation at liquid/solid interface in a thin Ga–In liquid layer with free surface, Ultrason. Sonochem. 71 (2021), 105356.
[48] W. Cui, C. Wang, J. Yan, Z. Wang, D. Wei, Wetting and reaction promoted by ultrasound between sapphire and liquid Al–12Si alloy, Ultrason. Sonochem. 20 (2013) 196–201.